Adhesion and adhesive transfer at aluminum/diamond interfaces: A first-principles study

Yue Qi and Louis G. Hector, Jr.
Materials and Processes Lab, GM R&D Center, Mail Code: 480-106-224, 30500 Mound Road, Warren, Michigan 48090, USA
(Received 4 December 2003; revised manuscript received 4 March 2004; published 3 June 2004)

Using a first-principles methodology, we investigated the effect of diamond surface termination on the work of separation (W_{sep}), interface geometry, bond character, and adhesive transfer of three Al/diamond interfaces, viz., Al(111)/C(111)-1×1, Al(111)/C(111)-2×1 and Al(111)/C(111)-1×1:H. Bond character was explored with the electron localization function. Adhesive transfer was investigated by subjecting each interface to a series of tensile strain increments up to fracture. This also allowed us to generate constitutive laws for decohesion and predict the interfacial strength. The highest adhesion occurs in Al(111)/C(111)-1×1 for which $W_{sep}=4.08$ J/m^2. Adhesion is due to strong covalent Al-C bonds, and two Al layers transfer to the diamond. Mixed covalent/metallic bonds form along Al(111)/C(111)-2×1, for which $W_{sep}=0.33$ J/m^2, and fracture occurs without adhesive transfer. Bond breaking in the clean interfaces is accompanied by a jump-to-separation process. We also find that Al(111)/C(111)-1×1 is energetically favored over Al(111)/C(111)-2×1 even though the latter contains reconstructed diamond. This suggests that the reconstruction of C(111)-2×1 is broken upon exposure to Al. For Al(111)/C(111)-1×1:H, we computed $W_{sep}=0.02$ J/m^2; no bonds form between Al and H and fracture occurs without adhesive transfer. Qualitative comparison of our results with existing experiments is also presented.

DOI: 10.1103/PhysRevB.69.235401 PACS number(s): 68.35.Gy

I. INTRODUCTION

Adhesion and adhesive wear are important to numerous applications in which various loadings are transmitted through different material interfaces. These applications range from microelectronics devices, hard coatings or thermal barrier coatings, where large adhesion is often desirable, to manufacturing of structural components, where minimal adhesion and adhesive wear are often desired. Modeling of adhesion at different material interfaces from first principles has largely focused on computing the work of separation, W_{sep}, which is the reversible work required to separate an interface into two free surfaces (neglecting plastic and diffusional degrees of freedom[1]). Specific interface couples that have been modeled are: BeO/diamond (Ref. 2), Al/β-SiC (Ref. 3), Al/AlN (Ref. 4), Nb/sapphire (Ref. 1), Al/α-Al_2O_3 (Ref. 5), Ni/Al_2O_3 (Ref. 6), Al/WC (Ref. 7), Al/VN (Ref. 8), Co/TiC(001) (Ref. 9), Fe/TiC (Ref. 10), and Cu/diamond (Ref. 11). In general, W_{sep} provides a useful measure of the strength with which two materials adhere to one another; however, it offers no detailed information about adhesive transfer due to an applied strain. In addition to knowing W_{sep}, it is important to know how the interfacial strength compares with the cohesion strength of the constituent materials and the only way to accomplish this is by imposing loads that lead to fracture.

We chose to study Al/diamond interfaces due to their broad applications, including Schottky diodes, field-effect transistors,[12] and in-plane gate transistors.[13] Another application that has received less attention is the design of adhesion-mitigating coating materials for Al forming. During many forming processes, the deformation kinematics and plasticity lead to the destruction of the natural Al oxide layer thereby exposing nascent Al. Once nascent Al adheres to a forming component surface, adhesive transfer of Al results as the two surfaces separate. This elevates forming temperatures and loads and typically leads to process termination. Various coatings have been applied to tool surfaces to inhibit Al adhesive transfer but most of these are largely unsuccessful.[14,15] Among them, crystalline diamond and amorphous diamond-like carbon (DLC) are the most promising wear-resistant tool coatings for low-temperature Al machining (for example) based on their unique tribochemical properties. One of the critical pieces of information that is often lacking when designing coating materials that either promote or inhibit Al adhesion is the nature of chemical bonding at the interface and how this impacts adhesive transfer which is the macroscale manifestation of chemical bonding (aside from surface texture).

Experimental study of adhesion of Al and diamond is extremely challenging since it is difficult to keep Al from oxidizing even in ultrahigh vacuum conditions.[16] In reported sessile drop measurements, pure Al droplets wet diamond with work of adhesion values in the 1.0–1.2 J/m^2 range.[17] At the present time, there are no published experimental studies of Al/diamond adhesion in a controlled environment similar to that reported for Cu/diamond,[18] which clearly show how diamond surface termination affects adhesion. Hence, further understanding is needed to control Al adhesion to diamond coatings with different surface terminations.

It has been demonstrated that the freshly cleaved C(111)-1×1 surface is unstable due to dangling surface bonds, and undergoes a reconstruction that effectively passivates the clean surface through reorganization of its electronic structure. It is now generally believed that the reconstructed, clean diamond (111) surface is a 2×1 "Pandey" π-bonded chain model.[12,19,20] The reconstructed surface, which consists of rows of π-bonded C atoms with sp^2 hybridization, has been the subject of several theoretical investigations. Among the more comprehensive of these studies is that due to Kern *et al.*[21] who predicted that C(111)-2×1 is lower in energy than C(111)-1×1 by approximately 0.79

eV/atom. Kern *et al.*[21] also demonstrated that H-terminated diamond (111)-1×1, which is found in diamond grown through chemical vapor deposition (CVD),[2] is 0.69 eV lower in energy than C(111)-2×1:H.

Although significant advancements have been made in understanding the clean diamond surface structure, as well as passivated diamond surfaces, there is a dearth of information about adhesion and adhesive transfer of Al to diamond surfaces. In addition, the possibility of interfacial reconstruction of C(111)-1×1 with Al has not been investigated experimentally. In a previous communication,[22] we examined the effect of H-passivated diamond on Al adhesion and adhesive transfer as compared with a clean C(111)-1×1 diamond surface. We did not, however, provide important details behind our W_{sep} calculations and the bond character at the interfaces. In addition, we did not extensively explore the effect of diamond reconstruction on Al adhesion and adhesive transfer, the corresponding bond character at the reconstructed interface, and the decohesion process under tensile straining. This precluded a careful comparison of adhesion and decohesion of interfaces of Al(111) with C(111)-1×1, C(111)-2×1, and C(111)-1×1:H. In the present work, we conducted an in-depth investigation of Al(111) adhesion and adhesive transfer to these three diamond surfaces. We focused on the details behind our W_{sep} calculations for each interface and analyzed interfacial bonding using the electron localization function (ELF). We then explored adhesive transfer by subjecting our interfaces to a series of tensile strain increments. The first-principles simulations revealed the atomic-scale details of the interfacial separation process for each interface and provided a stress-strain relation for decohesion of the interfaces. The bond character, diamond surface termination effect on adhesion and adhesive transfer, and decohesion process are carefully compared for each of the three diamond surface terminations and the structure of the Al/diamond interface as suggested by our computed energetics is discussed.

The remainder of this article is organized as follows: in Sec. II, the first-principles computational methodology used in this study is briefly summarized; Sec. III describes our computed bulk properties of Al and diamond; in Sec. IV, we present the computed surface energies of Al(111), C(111)-1×1, C(111)-2×1, and C(111)-1×1:H; in Sec. V, the model interfaces are described and adhesion is examined via calculating W_{sep}, the geometries of the relaxed interfacial structures are examined, and interfacial bonding is analyzed via contours of the ELF; Sec. VI examines the computed ideal strength σ_{max} of each interface and adhesive transfer due to the application of progressive tensile strain increments; in Sec. VII, we discuss our results within the context of related experimental work and address the issue of diamond reconstruction upon exposure to nascent Al; in Sec. VIII we summarize the major observations from this work.

II. COMPUTATIONAL METHODOLOGY

The Vienna *ab initio* Simulation Package (VASP) (Refs. 23, 24) was used to solve for the single-particle Kohn-Sham (KS) (Ref. 25) wave functions via a (high precision) plane-wave basis set.[26,27] VASP determines the KS ground state via an iterative, unconstrained band-by-band conjugate gradient minimization technique[28] and optimized charge-density mixing.[29,30] The generalized gradient approximation (GGA) of Perdew and Wang[31] was used for the exchange-correlation energy functional. Potentials based upon the all-electron projector-augmented wave (PAW) method of Blöchl[32] were used for C and H with core radii of $r_c = 0.873$ Å and $r_c = 0.582$ Å, respectively. A norm-conserving pseudopotential based upon the method of Rappe *et al.*[33] in the separable Kleinman-Bylander[34] form was used for Al with cutoff radius of 0.96 Å, since its cutoff energy is closest to those of the other elements in the cell compared with other Al potentials in the VASP repertoire. The *d projector* was chosen as the local component. Sampling of the irreducible wedge of the Brillouin zone (IBZ) was performed with a regular Monkhorst-Pack[35] grid of special **k**-points. To facilitate relaxation of the atomic forces, partial occupancies of the single-particle wave functions were introduced via the first-order method of Methfessel-Paxton[36] with an energy level broadening of $\sigma = 0.1$ eV. The associated energies were computed by extrapolating to $\sigma = 0$. Total energies of the optimized structures were computed with the linear tetrahedron method with Blöchl[37] corrections in order to eliminate any broadening-related uncertainties in the energies. Ground-state atomic geometries were obtained through minimization of the Hellman-Feyman[38] forces using a conjugate gradient algorithm. For all structures, the electronic degrees of freedom were converged to 10^{-5} eV/cell and the Hellman-Feyman forces were relaxed to less than 0.05 eV/Å. Total energy convergence of 1–2 meV/atom was obtained with a 400 eV plane-wave cutoff energy.

III. BULK PROPERTIES

As a check of the computational methodology, we computed selected bulk properties of crystalline Al and diamond (space groups $Fm\text{-}3m$ and $Fd\text{-}3m$, respectively), and tabulated these results, along with available experimental values in Tables I and II. The ground-state lattice constant a_o, single-crystal bulk modulus B_o, and cohesive energy E_{coh} (referenced to the spin-polarized atoms) were computed by fitting $E(V)$ data to the Murnaghan equation of state.[39] Elastic constants and the Voigt-Reuss-Hill (VRH) (Ref. 40), polycrystalline moduli (B_{VRH}, bulk modulus; G_{VRH}, shear modulus; Y_{VRH}, elastic modulus), which are the averages of the corresponding Voigt and Reuss moduli, were computed for the VASP-optimized (0 K) structures using the least-squares fitting method of LePage and Saxe.[41] In this method, the stresses computed in the VASP code[42] serve as inputs to a least-squares fit of the unknowns appearing in the equations describing the linear stress-strain relationships for a selected sequence of strains applied in specific directions. For Al and diamond, the unknowns are the three independent elastic constants (C_{11}, C_{12}, and C_{44}) for cubic symmetry.[43] The elastic constants were derived from the first derivatives of the stresses (computed by VASP) with respect to strain, rather than from the second derivatives of the total energy with respect to strain. The method therefore avoids the nu-

TABLE I. Comparison of DFT GGA-calculated Al bulk properties with room temperature and 0 K (where available) experimental values.

Property	Calculated	Experiment at 298.15 K (0 K)
a_o (Å)	4.04	4.05 (Ref. 45)
B_o (GPa)	72.1	72.2 (Ref. 46), (79.4) (Ref. 45)
E_{coh} (eV)	3.56	(3.39) (Refs. 47 and 48)
C_{11} (GPa)	107.3	114.3 (112.9) (Ref. 46)
C_{12} (GPa)	54.5	61.9 (70.8) (Ref. 46)
C_{44} (GPa)	28.2	31.6 (30.9) (Ref. 46)
B_{VRH} (GPa)	70.9	76 (79.4) (Ref. 46)
G_{VRH} (GPa)	27.2	26 (29) (Ref. 46)
Y_{VRH} (GPa)	72.3	70 (78.3) (Ref. 46)
C_v (J/mol/K)	22.8	24.2 (Ref. 46)
Θ (K)	428	428 (Ref. 47)

merical difficulties often encountered with evaluation of the second derivatives. Note that the elastic constants depend sensitively on the chosen **k**-point mesh. For convergence within 1–2 GPa for each modulus, we used 4060 and 455 **k**-points in the IBZ for the unstrained Al and diamond structures, respectively. The vibrational heat capacity at 298 K, C_v, and Debye temperature Θ were computed with the Debye model following the method outlined in Ref. 44. In most cases, the agreement between our theoretical calculations and reported experimental values is reasonable.

IV. SURFACE PROPERTIES

To determine the slab thickness needed for the interface structures, we conducted surface energy convergence tests on Al(111) and C(111) slabs to ensure that the constituent slabs simulated a bulk effect. In all surface models, a 10 Å vacuum was used in order to avoid interactions with periodic images. We used the method of Boettger[54] to compute surface energies. Each of the computed surface energies is summarized in Table III.

TABLE II. Comparison of DFT GGA-calculated diamond bulk properties with room temperature and 0 K (where available) experimental values.

Property	Calculated	Experiment at 298.15 K (0 K)
a_o (Å)	3.57	3.57 (Ref. 50)
B_o (GPa)	429.7	443 (Ref. 47)
E_{coh} (eV)	7.91	7.34 (Ref. 49)
C_{11} (GPa)	1058.6	949 (Ref. 46), (1080.5) (Ref. 51)
C_{12} (GPa)	129.2	151 (Ref. 46), (124.6) (Ref. 51)
C_{44} (GPa)	561.1	521 (Ref. 46), (579.4) (Ref. 51)
B_{VRH} (GPa)	438.9	417 (Ref. 52)
G_{VRH} (GPa)	520.3	468.2 (Ref. 52)
Y_{VRH} (GPa)	1118.8	1022.1 (Ref. 52)
C_v (J/mol/K)	5.6	6.11 (Ref. 49)
Θ (K)	2358.0	2200 (Ref. 53)

TABLE III. Surface energy vs slab thickness for various surfaces.

System	Ambient μ (eV)	No. of layers	Surface energy (J/m^2)
		3	0.75
Al(111)	—	5	0.78
		7∼10	0.76
C(111)-1×1	—	5∼10	5.66
		5	3.35
C(111)-2×1	—	6	3.38
		7∼8	3.35
C(111)-1×1:H	H, −1.12	5∼10	−7.56
	CH_4, −3.75	5∼10	0.04

A. Al(111)

The Al(111) surface has the densest packing and lowest surface energy. Energy convergence in the 1–2 meV per atom range was obtained with a **k**-point sampling of 37 **k** points (18×18×1, Γ centered) in the IBZ using a 270 eV plane-wave cutoff energy. We computed the surface energy of slabs ranging from 3 to 11 layers with three atoms per layer. We found that the surface energy was converged for a five-layer slab at 0.78 J/m^2 (0.27 eV/surface atom). We also computed the surface energy for the unstrained Al(111) having one atom per layer and found the converged value at the five-layer slab to be identical to that reported in Table III for the slightly strained slab used in the interface models. Further discussion of first-principles computations of the Al(111) surface may be found in Ref. 5.

B. C(111)-1×1

For the diamond slabs, energy convergence in the 1–2 meV per atom range was obtained with a **k**-point sampling of 12 **k**-points (8×8×1, Γ-centered) in the IBZ using a 400 eV plane-wave cutoff energy. We computed the surface energy of slabs ranging from 5 to 10 bilayers, with four C atoms per layer. We found that the surface energy was converged for a five-bilayer slab to 5.66 J/m^2 (1.95 eV/surface atom). We also found the same surface energy using diamond slabs with smaller surface areas. As a check of our calculations against the results of Kern *et al.*,[21] who computed the surface energy of C(111)-1×1 using an ultrasoft pseudopotential for C with the local-density approximation (LDA), we recomputed the surface energy using a C pseudopotential constructed with the PAW method using LDA. Our computed surface energy of 6.26 J/m^2 (2.16 eV/surface atom) is identical to that reported by Kern *et al.*[21]

C. C(111)-2×1

We built C(111)-2×1 based on Pandey's structure,[20] followed by atomic relaxation to obtain the minimized surface energy. Energy convergence in the 1–2 meV per atom range was obtained with a **k**-point sampling of 34 **k**-points (8×8×1, Γ-centered) in the IBZ using a 400 eV plane-wave cutoff energy. We found that the surface energy was converged

for a five-bilayer slab to 3.35 J/m^2 (1.16 eV/surface atom). Note that Kern *et al.*[21] computed the surface energy of C(111)-2×1 to be 3.97 J/m^2 (1.356 eV/surface atom) using an ultrasoft pseudopotential for C with LDA. Generally, the surface energy calculated from LDA method is larger than the GGA results due to LDA overbinding.

D. C(111)-1×1:H

The C(111)-1×1:H surface was created by terminating each surface C atom with a single H atom. The surface energy in this case is somewhat more problematic to compute than it is for the clean surfaces since it depends upon the H chemical potential, and hence the ambient reference material which serves a source of H becomes important.[55] We computed the surface energy for C(111)-1×1:H assuming ambient references of H (atomic hydrogen) and CH_4 via

$$E = E_{\text{slab}} - (n_C \mu_C + n_H \mu_H), \tag{1}$$

where E_{slab} is the slab energy, n_C and n_H are the numbers of C and H atoms in the H-terminated slab, respectively, and μ_C and μ_H are the corresponding chemical potentials for C in diamond and atomic hydrogen, respectively. Our numerical results indicate that the surface energy is converged for a H-terminated slab with five bilayers. Note that the negative surface energy for the H ambient implies that it is energetically favorable to make new surface. This is not surprising since atomic hydrogen etches diamond surfaces.[56,57] However, a stable surface is formed from the CH_4 reference, which is the source gas of CVD diamond growth, and the resulting surface energy [calculated via Eq. (1)] of 0.04 J/m^2 (for the five-bilayer slab) due to hydrogen adsorption is substantially lower than the corresponding value of 5.66 J/m^2 for the clean (unstable) surface.

V. INTERFACES

A. Mismatch and registry

Due to the substantial lattice mismatch (13%) between Al and diamond, it was not possible to construct interfaces with perfect registry (i.e., with all surface Al atoms atop surface C atoms). To minimize the mismatch between our constituent slabs, we used four C atoms/layer in C(111) and three Al atoms/layer in Al(111), and overlapped Al $\langle 11\bar{2}0\rangle$ with C $\langle 10\bar{1}0\rangle$. This reduced the mismatch to less than 2% and allowed us to ignore misfit dislocations. To improve interface commensuration, the in-plane cell dimensions of the as-cleaved Al(111) slabs were slightly increased to match the surface area of the diamond slabs (22.12 Å^2) following the coherent interface approximation.[58] This represented a small strain to Al(111) that did not significantly affect any of the computed energies. The resulting interfaces were therefore not fully coherent (i.e., registry was imperfect) with the diamond surface, since the three Al(111) surface atoms cannot all simultaneously be exposed to the same chemical environment due to four C surface atoms.

We explored two different registries for each interface and these are shown in Figs. 1(a)–1(d), where the Al atoms are

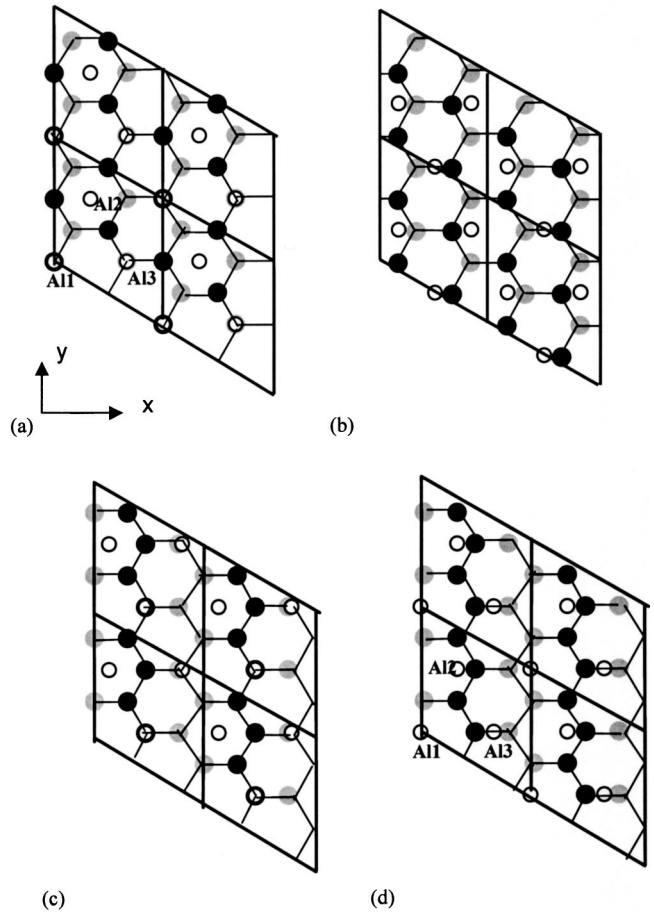

FIG. 1. Interface matching. Atom shading: Al circle, C-black dot (1st layer), and gray dot (2nd layer). (a) is partially coherent Al(111)/C(111)-1×1, (b) is fully incoherent Al(111)/C(111)-1×1, (c) is partially coherent Al(111)/C(111)-2×1, and (d) is fully incoherent Al(111)/C(111)-2×1.

open circles, atoms in the top diamond layer are black, and the next (subsurface) layer of diamond atoms are gray. Figure 1(a) shows the partially coherent registry for Al(111)/C(111)-1×1 (also appropriate for Al(111)/C(111)-1×1:H), in which only one Al surface atom sits atop a surface C atom. Figure 1(b) shows the second registry, which is fully incoherent, with Al atoms lying above holes in the first and second diamond layers. As a consequence of coherency, the three Al surface atoms (which we label as Al1, Al2, and Al3) sit in three different chemical environments in both registries. For example, in Fig. 1(a), which is the partially coherent registry for Al(111)/C(111)-1×1, atom Al1 sits atop a C atom in the top diamond surface layer; atom Al2 sits in the center of three C atoms in the top diamond surface layer; atom Al3 sits atop a C atom in the second diamond surface layer. The interface registries for Al(111)/C(111)-2×1 are shown in Figs. 1(c) and 1(d) with the zig-zag, π-bonded chains of C atoms in the top diamond layer. Figure 1(c) shows the partially coherent registry where only one Al surface atom sits atop a surface C atom. Figure 1(d) shows the fully incoherent registry where no Al surface atoms sit atop C surface atoms. Rather, atom Al1 sits near three atoms in the C chain of the

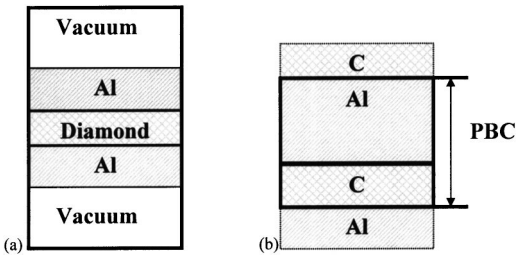

FIG. 2. Two interface models, (a) vacuum cell with in-plane periodicity and (b) dense cell with fully periodic boundary conditions (PBC).

second diamond layer, Al2 sits near three atoms in the C chain of the top layer, and Al3 sits atop the tilted bond between C atoms in first two layers.

In our calculations, we found that interface registry has a negligible impact on adhesion since our W_{sep} values differed by less than 0.5% for each interface pair [e.g., Al(111)/C(111)-1×1, partially coherent and fully incoherent]. We therefore focused only on the partially coherent interfaces for Al(111)/C(111)-1×1 and Al(111)/C(111)-1×1:H, and the incoherent interface for Al(111)/C(111)-2×1, which are slightly lower in energy than their counterparts, and are likely to contain the strongest interfacial bonds. Note that we shall omit (111) in the interface designations throughout the remaining text.

B. Simulation cells

Using the Al(111) and C(111) slabs initially cleaved with the VASP-computed lattice constants given in Tables I and II, we constructed two types of cells, viz., vacuum and dense cells; these are shown schematically in Fig. 2. In the vacuum cell [Fig. 2(a)], a C(111) slab was sandwiched between two Al(111) slabs. The slabs, which were surrounded with 10 Å of vacuum to preclude interactions between free surfaces, had in-plane periodicity. The dense cell [Fig. 2(b)] was fully periodic since no vacuum was introduced into the cell. It consisted of alternating C(111) and Al(111) slabs. All cells were constructed to have (at the very least) $P-1$ (inversion) symmetry to ensure that the two interfaces were identical and the interfacial energy was uniquely defined. The symmetry also precluded a dipole moment in the cell (which would be time consuming to correct in the calculations, but would nevertheless distort the computed energies) and nonphysical electrostatic coupling between the interfaces.

Energy convergence in the 1–2 meV per atom range was obtained with a **k**-point sampling of 12 **k**-points ($8\times8\times1$, Γ-centered) in the IBZ using a 400 eV plane-wave cutoff energy. For the two types of cells, we used two different methods for determining the slab thicknesses required to simulate a bulk effect. This is very important, since the computed W_{sep} values can dramatically differ for interfaces that simulate thin films in contrast to those that simulate a bulk effect. For the vacuum cells, the slab thickness was determined via convergence of the surface energy of each material as discussed above, and based upon these results we chose a six-bilayer C(111) slab and two five-layer Al(111) slabs. For the dense cells, the slab thickness was chosen based upon convergence of the interfacial energy H_i, which is defined as

$$H_i=\tfrac{1}{2}[H_s-(N_{Al}H_{Al}+N_CH_C)]. \quad (2)$$

The total energy of the cell is H_s, N_{Al} and N_C are the numbers of layers of Al(111) and C(111), respectively, and H_{Al} and H_C are the energies per layer for Al(111) and C(111), respectively. We varied the thickness of both Al(111) and C(111) layers until the change in H_i was less than 0.01 J/m^2. The computed interfacial energies for various slab thicknesses are listed in Table IV; these were calculated from the unrelaxed structures with interfacial separation of 2 Å, and hence they were pertinent only for the convergence tests. We found six bilayers of diamond and 10 layers of Al led to a converged interfacial energy. The two convergence methods gave the same results for the slab thickness. Both the vacuum cell and dense cell contained 30 Al (two slabs with five layers) and 48 C atoms (6-bilayers), with 8 H surface atoms terminating the C surface atoms in Al/C-1×1:H.

TABLE IV. Interface energy vs slab thickness for fully periodic Al/C interface structure.

No. of C bilayers	No. of Al layers	No. of atoms	Interfacial energy (J/m^2)
4	4	44	2.44
4	7	53	2.48
4	10	62	2.46
4	13	71	2.46
5	4	52	2.49
5	7	61	2.49
5	10	70	2.46
5	13	79	2.46
6	4	60	2.54
6	7	69	2.49
6	10	78	2.45
6	13	87	2.45

C. W_{sep}

The standard definition of W_{sep} is

$$W_{sep}=\sigma_{1v}+\sigma_{2v}-\sigma_{12}=(E_1^{tot}+E_2^{tot}-E_{12}^{tot})/A, \quad (3)$$

where σ_{iv} is the surface energy of the slab i, σ_{12} is the interface energy, E_i^{tot} is the total energy of slab i, and E_{12}^{tot} is the total energy of the interface system with slab materials 1 and 2, and A represents the total interface area. Both vacuum and dense cells were expected to yield essentially the same W_{sep} values.

Calculation of W_{sep} and the minimum interfacial energy required relaxation of the interface structures. For the vacuum model, it was necessary to relax the atomic coordinates without changing the cell shape since the atomic layers relaxed into the free space afforded by the vacuum regions above and below the interface. The initial interfacial separation between the Al and diamond slabs in the vacuum cells was set at 1.5 Å; this distance subsequently changed during

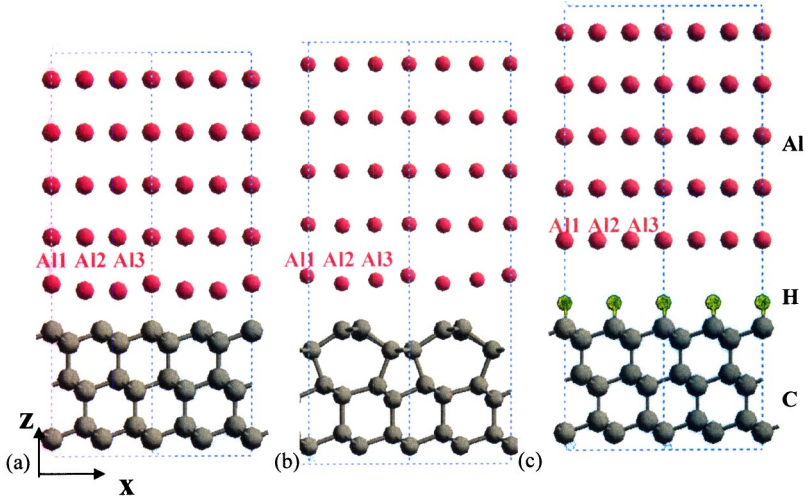

FIG. 3. (Color online) Relaxed interfaces projected along the y direction: (a) Al(111)/C(111)-1×1 ($a=b=5.027$ Å, $c=34.815$ Å), (b) Al(111)/C(111)-2×1 ($a=b=5.027$ Å, $c=36.7145$ Å), (c) Al(111)/C(111)-1×1:H ($a=b=5.018$ Å, $c=40.075$ Å).

relaxation. For the dense cells, this required minimization of both the cell volume and atomic coordinates. We constructed dense cells over a range of cell volumes, followed by relaxation of the atomic coordinates in each cell without changing the volume and shape of the cell. We then chose that structure which gave the minimum energy (or zero pressure) as the relaxed interface structure. This altered the cell shape to $a=b=5.027$ Å, $c=34.815$ Å for Al/C-1×1 and $a=b=5.018$ Å, $c=40.075$ Å for Al/C-1×1:H. For Al/C-2×1, the cell stresses along the x and y directions were unequal due to the zig-zag surface chains formed along the y direction. Hence, to maintain the symmetry we took the optimized cell dimensions along x and y in Al/C-1×1 for Al/C-2×1, which were $a=b=5.027$ Å, $c=36.4755$ Å.

The calculated W_{sep} values from the vacuum cells are: $W_{sep}=3.98$ J/m^2 for Al/C-1×1, $W_{sep}=0.42$ J/m^2 for Al/C-2×1, and $W_{sep}=0.02$ J/m^2 for Al/C-1×1:H. From the dense cells, we obtained: $W_{sep}=4.08$ J/m^2 for Al/C-1×1, $W_{sep}=0.33$ J/m^2 for Al/C-2×1, and $W_{sep}=0.02$ J/m^2 for Al/C-1×1:H. Note that the dense and vacuum cell models with clean diamond differ in their associated W_{sep} values by about 0.1 J/m^2; this trend was noted for all interfaces. The nearly identical W_{sep} values computed for the two cell types demonstrated the validity of our approach and for this reason, the remaining discussion will focus only on results obtained from calculations on the dense cells.

The reconstruction of the diamond surface will also change the value of W_{sep} for Al/C-1×1. We computed $W_{sep}=4.08$ J/m^2, assuming the unreconstructed diamond surface is C(111)-1×1. However, as discussed earlier, this termination is unstable to reconstruction, and if we assume that the free surfaces corresponding to Al/C-1×1 are Al(111) and C(111)-2×1, W_{sep} is subsequently reduced from 4.08 J/m^2 to 1.77 J/m^2. This reduction in W_{sep} does not, however, change the interfacial energy of Al/C-1×1. Following the definition of W_{sep}, we believe that Al/C-1×1 would first separate, with the fresh C(111)-1×1 surface then reconstructing to C(111)-2×1. Therefore, we maintain that separation of the Al/C-1×1 along the plane between the Al and C slabs requires an energy per unit area of 4.08 J/m^2.

D. Relaxed interface structures

Figure 3 compares the optimized interface geometries projected on the xy plane from the dense cell models. Since the cells are symmetric, we show one-half of each cell and hence a single interface. The Al interface atoms changed their atomic geometries under the effect of diamond surface atoms. For example, relaxation of the atomic forces in Al/C-1×1 and Al/C-2×1 caused a rippling of the Al surface atoms. Rippling in Al/C-1×1 [Fig. 3(a)] results from the movement of Al1 away from the clean diamond surface, while Al2 and Al3 moved towards the diamond surface.[22] The average distance between the Al and diamond at the interface was 1.86 Å. The average interlayer spacings in the first three layers of the Al slab were $D_{1-2}=2.22$ Å, $D_{2-3}=2.25$ Å, and $D_{3-4}=2.27$ Å. Along Al/C-2×1 [Fig. 3(b)], Al1 moved away from the diamond surface, while Al2 and Al3 moved towards the diamond surface, and the average distance between the Al and C interface atoms was 2.16 Å. No rippling of the Al surface atoms occurs along Al/C-1×1:H [Fig. 3(c)] and the average distance between the Al and H surface layers increased to 3.21 Å, which is larger than the 2.33 Å interlayer spacing of Al(111).[22] Wang and Smith[11] observed a similar repulsion of Cu by H-terminated diamond. We noted a decrease in the separation to 2.64 Å when optimizing with LDA, which is still larger than the interlayer spacing of Al. The smaller separation at the LDA-optimized interface is therefore due, in part, to LDA overbinding, but this does not significantly change adhesion along Al/C-1×1:H.

E. ELF analysis

Although there are different ways of qualitatively exploring interfacial bond character, we employed the electron localization function (ELF). Note that the ELF is a position-dependent function with values that range from 0 to 1; ELF=1 corresponds to localization (i.e., a covalent bond), and ELF=0.5 corresponds to electron-gas-like pair probability (i.e., a metallic bond).[59] The ELF is undefined for values

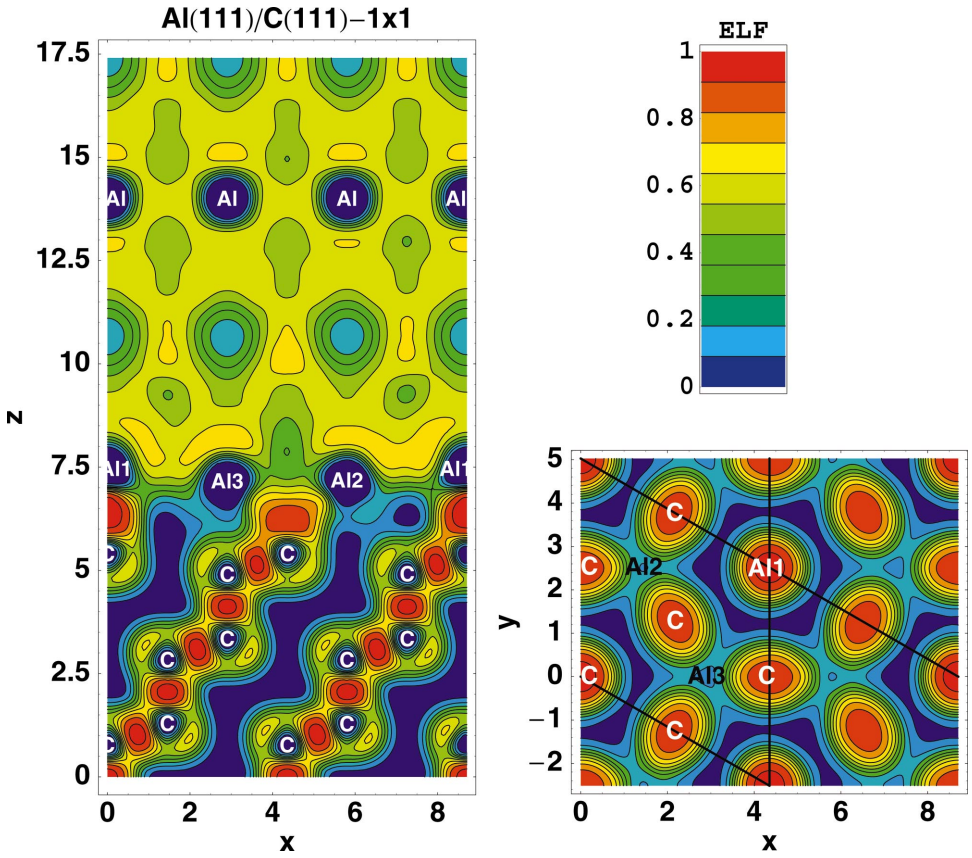

FIG. 4. (Color) ELF contour plots of optimized Al(111)/C(111)-1×1. (a) along the *xz* plane and (b) along the *xy* plane.

less than 0.5. We found that the ELF is particularly useful for Al/diamond interfaces since diamond is covalently bonded and Al is metallic.

Figures 4–6 are ELF contour plots that reveal the complicated bonding environment at the Al/diamond interfaces. Specific ELF values are color coded according to the figure legends, with ELF=1 corresponding to red, ELF=0.5 corresponding to a yellow-green, and ELF=0 corresponding to blue, which are regions of undefined ELF (e.g., the Al and C atomic cores or interstitial regions in the diamond slab). We also marked the atomic positions in each figure; the interface Al atoms are again specified as Al1, Al2, and Al3.

Figure 4(a) is an ELF contour plot for Al/C-1×1 cleaved along the *xz* plane passing through the cell origin; the labeled atom cores are in the cleaved *xz* plane. Figure 4(b) shows ELF contours in the cleaved *xy* plane slicing through Al-C bonds (this is actually the midplane between the Al and C atoms at the interface); hence, the labeled Al atoms are above the *xy* plane and the labeled C atoms are below the *xy* plane. The covalent bonds between the C atoms in the diamond slab are clearly indicated by the regions of high ELF (red) that wind to the bottom of the slab in Fig. 4(a). These are surrounded by regions of lower localization that represent components of the three-dimensional sp^3 bond character in diamond. Interfacial bonding shows strong covalent character as indicated by the distribution of ELF values across the colored contour patterns. The strongest covalent bond is formed between Al1 and the C atom directly below it (the coherent pair) as denoted by the red ELF region between these atoms (ELF=0.9–1.0). The incoherent Al2 and Al3 also formed covalent bonds with C atoms, which are weaker (ELF=0.8–0.9) than those formed between the coherent pair. In the *xy* plane shown in Fig. 4(b), the covalent pair Al1-C shows a symmetric sphere of ELF, and the ELF contours due to the incoherent pair are elongated along two Al atoms (Al2 and Al3), since the bond is shared by one C atom and two Al atoms. Examination of the partial density of states for Al2 and Al3 with bulk Al atoms allowed us to conclude that the covalent bonds result from Al and diamond *p* states at the interface, and the diamond surface shows local metallic character.

Figure 5 reveals the bonding environment along Al/C-2×1. Figure 5(a) shows ELF contours on a cleaved *xz* plane passing through the origin, and Fig. 5(b) shows ELF contours on a cleaved *xy* plane slicing through Al-C bonds. Interfacial bonding clearly has a mixed covalent/metallic character as indicated by the distribution of ELF values across the colored contour patterns in Fig. 5(a). For example, the strongest covalent bond at the interface is formed between Al3 and C surface atoms and is denoted by the red ELF region between these atoms (ELF=0.9–1.0). This is confirmed by the view shown in Fig. 5(b) where a region of high ELF corresponds to the bond between Al3 and one C. Recall that Al3 lies above the tilted bond between a C atom in the diamond surface layer and a C atom in the second layer [see Fig. 1(d)], so the Al-C bond is formed between Al3 and a C surface atom. On the other hand, there is essentially no localization between Al1 and C atoms in the diamond indicating the absence of covalent bonding. This is shown in Fig. 5(b), since regions of low ELF surround the position of Al1.

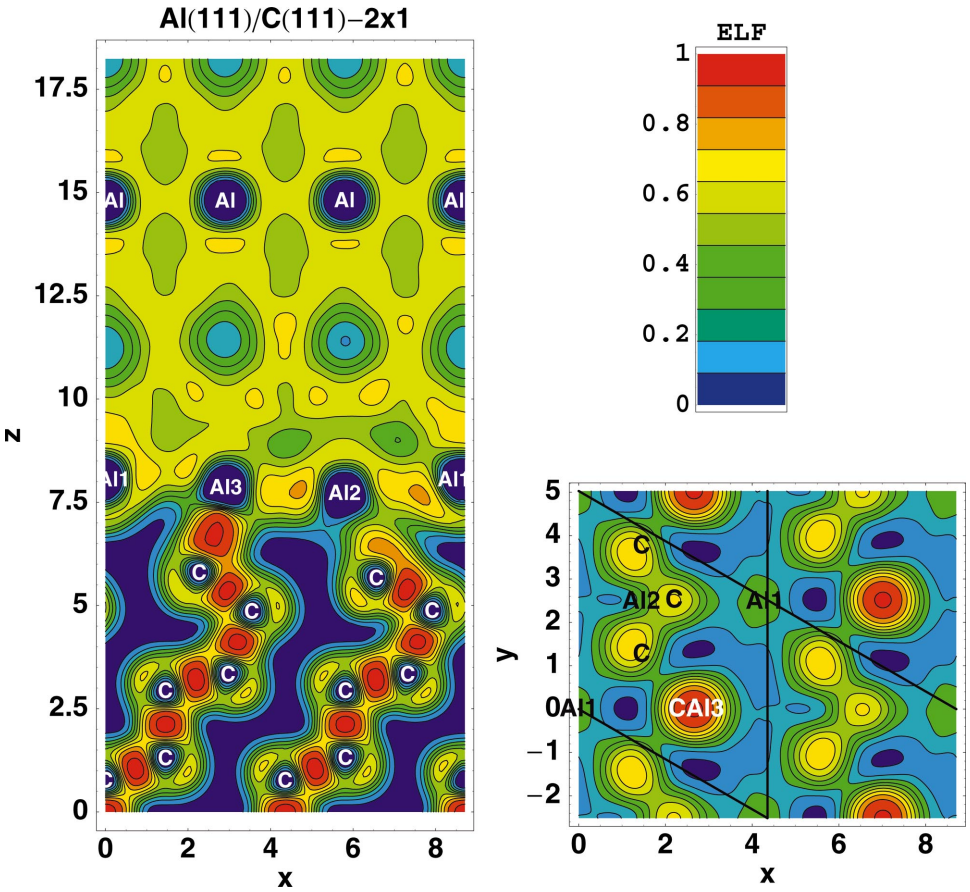

FIG. 5. (Color) ELF contour plots of optimized Al(111)/C(111)-2×1. (a) along the *xz* plane and (b) along the *xy* plane.

Note that Al1 sits above three atoms in the subsurface layer of C as shown in Fig. 1(d). Finally, Al2 forms bonds with mixed covalent/metallic character with three surface C atoms since the maximum ELF value is close to 0.7–0.8. This is shown in Fig. 5(b) as the yellowish regions (ELF~0.8) that partially surround the Al2 position. Small regions of localization between Al3 and Al2, and Al2 and Al1 are shown in Fig. 5(a). This is an indication that there is some degree of covalency in the Al surface layer due to bonding with C surface atoms and it further demonstrates the mixed covalent/metallic bonding along Al/C-2×1.

Figure 6 shows that the strongest covalent bonds along Al/C-1×1:H are formed between H and C pairs; the ELF is undefined between the H and Al layers which implies the absence of covalent, metallic, and ionic bond character. The only possible interactions are dispersion interactions which are not accurately described by the implementation of density functional theory (DFT) in the VASP code.

VI. INTERFACIAL STRENGTH AND ADHESIVE TRANSFER

Adhesive transfer was explored through application of tensile strain increments to each cell. Starting with the minimum-energy structure as the reference state (0% strain state), the interface couples were uniformly elongated at a set strain increment, followed by minimization of all atoms to obtain the relaxed geometries. The strain was then incremented and the process continued up to fracture (i.e., when two free surfaces formed). During the simulations, the strain was applied only along the *z* direction (perpendicular to the interface), while the cell lengths along the *x* and *y* directions were fixed.

A. Adhesive transfer

Figure 7 shows the fractured interface geometries for all three interfaces, where the distances between the two free surfaces are at least 5 Å apart. Figure 7(a) shows that adhesive transfer occurred in Al/C-1×1, since two layers of Al adhered to the diamond surface. This result is consistent with the correspondingly large W_{sep} and the strong covalent interfacial bonds observed in the ELF contours. In this case, adhesion leads to adhesive transfer during tensile straining. On the other hand, H-passivated diamond does not bond with Al and thus no adhesion occurs as shown in Fig. 7(c), which is expected from the negligible W_{sep} (0.02 J/m^2) value for Al/C-1×1:H. Tensile straining of Al/C-2×1, resulted in fracture without adhesive transfer, as shown in Fig. 7(b): the newly formed diamond free surface remains the Pandey reconstructed surface. This indicates that the adhesive bond strength (which is mixed covalent/metallic) is less than the cohesion strength of Al, and decohesion occurs at the interface rather than in the Al. Thus Al/C-2×1 represents another category of interface wherein adhesion is not sufficient enough to cause adhesive transfer during tensile straining.

The cohesion energy of bulk Al is approximately twice the Al(111) surface energy, which is about 1.52 J/m^2 and

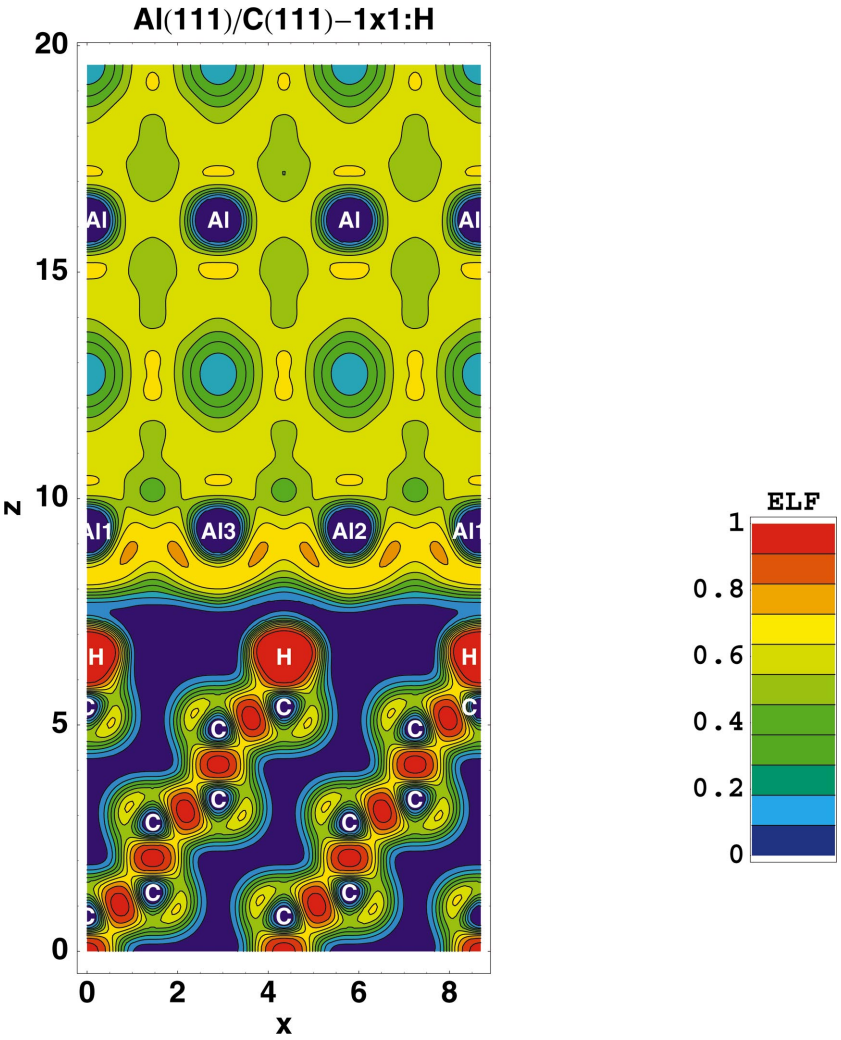

FIG. 6. (Color) ELF contour plot of optimized Al(111)/C(111)-1×1:H along the *xz* plane.

W_{sep} at Al/C-1×1 is much larger than the cohesion energy of bulk Al. Alternatively, W_{sep} at Al/C-2×1 and Al/C-1×1:H are less than the cohesion energy of bulk Al. Based upon these observations, it is tempting to infer from the W_{sep}/Al cohesion energy ratio that adhesive tranfer is more likely for Al/C-1×1, less likely for Al/C-2×1, and certainly improbable for Al/C-1×1:H. However, before such a comparison can be meaningfully used to infer adhesive transfer

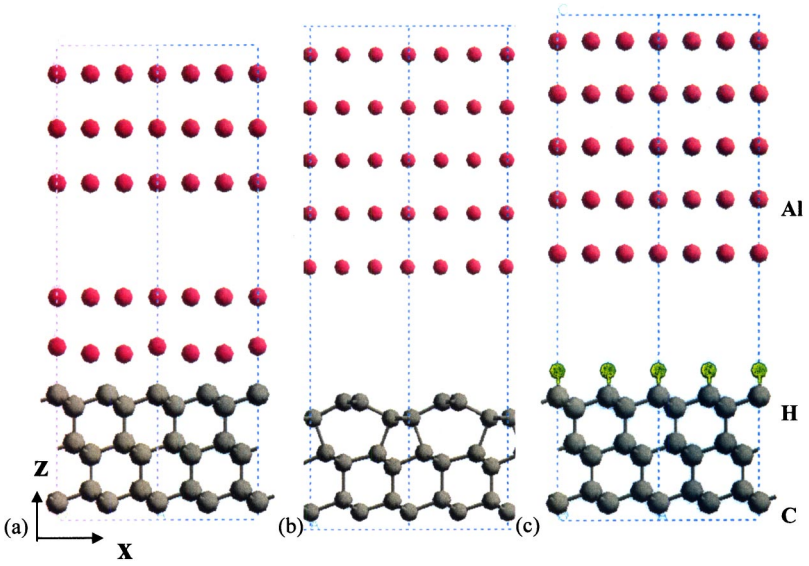

FIG. 7. (Color online) The fractured interface structure of (a) Al(111)/C(111)-1×1 showing two Al transfer layers, (b) Al(111)/C(111)-2×1, and (c) Al(111)/C(111)-1×1:H without adhesive transfer.

in a general sense, additional interfaces for which W_{sep} and the cohesion energy of the weaker material are very close should be examined (see Ref. 8, for example). Even if this ratio is ultimately proven to be useful for predicting adhesive transfer at the atomic scale, prediction of the precise amount of adhered material and its relaxed geometry remains problematic.

B. Debonding and jump to separation

In Fig. 8(a), we tracked the strain localized at the average interlayer distance between the fractured surfaces with respect to the strain of the unit cell. We note from Fig. 8(a) that interfacial separation is not a continuous process for Al/C-1×1 and Al/C-2×1 since there are three distinct regimes in the curve. The first regime involves linear deformation with all material being elastically stretched and elastic energy being stored in the system. For Al/C-1×1, the first regime extends from the original cell at 0% strain to 11.6% strain, and for Al/C-2×1, the elastic regime extends from 0% strain to 6.6% strain. The second regime is the jump-to-separate regime where the applied tensile stress exceeds the interfacial tensile yield strength and a large jump (denoted by the steep slope) occurs in the interlayer distance. For Al/C-1×1, the second regime extends from 11.6% to 14.5% strain, and is due to the onset and ultimate decohesion of the Al as two (new) free Al surfaces are formed. For Al/C-2×1, the second regime extends from 6.6% to 12.1% strain, and is due to the separation of Al from diamond. In both interfaces, the large jump in the interlayer distance is due to the onset and ultimate separation at the interface as two (new) free surfaces are formed; at the same time all the strain stored between each layer is released then localized at the distance between two free surfaces. This jump-to-separate process has some similarity with the jump-to-contact process found by Smith *et al.*[60] In both cases, the interface bonds (bonding or debonding) lead to a jump in the interface spacing.

The third regime involves full separation where two (new) free surfaces have formed, and the strain of the cell is then localized at the fractured surfaces; therefore the slope of the localized strain in the interface vs strain relationship for the whole cell is unity.

The interfacial distance at Al/C-1×1:H is a smooth line with slope of unity during the separation process. No jump to separation is observed, which indicates no debonding during separation, consistent with our finding that no interfacial bonds are formed.

C. Interface strength

We define the work of decohesion as the energy difference (per unit surface area) between the fractured system and the interface structure at a zero stress state. This was computed to be 1.56 J/m^2 for Al/C-1×1 and is the maximum E/A value of the topmost curve in Fig. 8(b) (which shows our computed energies per area for the three interfaces after each strain increment). If fracture were to occur exactly at the interface, as assumed when computing W_{sep}, it would require 4.08 J/m^2 to separate. The W_{sep} is therefore 2.5 times larger than the work of decohesion: this reveals that it is energetically more favorable for the system to fracture within the Al slab than at the interface. The middle two curves in Fig. 8(b) correspond to Al/C-2×1. The topmost of these shows that there is an energy barrier during the separation of the two interfaces, which was about 0.49 J/m^2; this is almost 50% more than the computed 0.33 J/m^2 W_{sep} value. This barrier is caused by metastable structures formed during separation. As shown in the lower curve of the two middle curves, when the two free surfaces approach each other in the reverse process, there is no such energy barrier. The bottom-most curve in Fig. 8(b) corresponds to Al/C-1×1:H and shows that the energy change during tensile straining is close to zero: this is consistent with the very small W_{sep}.

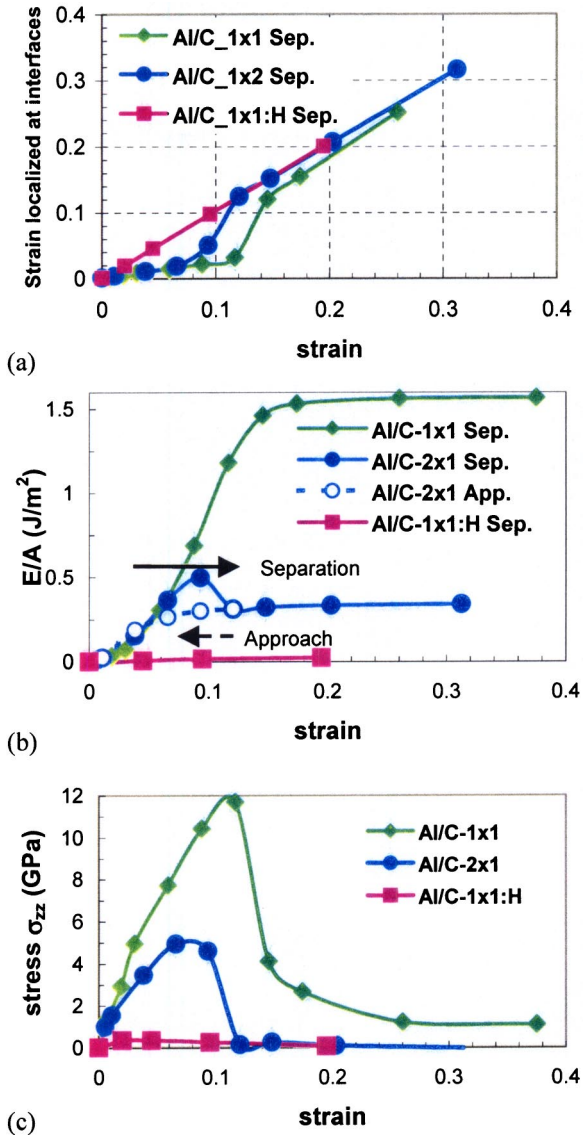

FIG. 8. (Color online) (a) Strain localized at two interfaces, (b) energy per area (E/A, J/m^2), and (c) stress variations with strain.

For Al/C-1×1, we have calculated the work of decohesion to be 2.25 J/m^2 with one Al transfer layer and 1.60 J/m^2 with three Al transfer layers. We also tested the possibility of

one or two Al transfer layers to the reconstructed diamond surface and found these structures to have work of decohesion values of 2.93 J/m^2 and 3.10 J/m^2, respectively. They are energetically unfavorable relative to the two Al transfer layers to the unreconstructed diamond surface. These calculations confirmed that transfer of two Al layers corresponds to a global energy minimum at Al/C-1×1. The decohesion energy and W_{sep} are the same at Al/C-2×1, since its fracture occurs without adhesive transfer, as shown in Fig. 6(b); the energy difference between the final separated two materials and the relaxed interface is exactly W_{sep}.

The calculated stresses in VASP have less precision than the energy, because the energy is calculated variationally. A consequence of this is that the minimum energy state does not always correspond to a zero stress state. Within the calculation error, we set the stress as zero for the minimum energy state and reported the stress increase after each strain increment in Fig. 8(c), which shows constitutive laws for interfacial decohesion. As a rough check, we have calculated the stress as the derivatives of the energy with respect to the strain, and the results are close to the VASP-calculated stresses as in Fig. 8(c).

Since fracture occurred inside the Al(111) slab as Al/C-1×1 was strained, failure resulted from decohesion of the softer of the two materials. However, it is not clear whether the yield stress of the interface is the same as the yield strength of pure Al. Due to the small model size, no plastic deformation was allowed and the theoretical cohesion strength can be calculated via $\sigma_{max}=\sqrt{E\gamma/d}$, where E is Young's modulus, γ is surface energy, and d is the interplanar spacing along the tensile axis.[61] Using our VASP-computed values of $E=72.3$ GPa (defined as Y_{VRH} in Table I), $d=4.04$ Å and $\gamma=0.76$ J/m^2 (Table III) for Al, we find $\sigma_{max}=15.3$ GPa. The topmost curve in Fig. 8(c) shows that the maximum tensile strength for Al/C-1×1 is 12 GPa, which is less than the theoretical tensile strength of bulk Al due to the effect of interface bonds. Thus we define the interface strength as the stress associated with incipient separation at/near the interface, to distinguish the ideal strength of the interface structure from the cohesive strength of the bulk material. The calculated interfacial strength is therefore 12 GPa for Al/C-1×1. For Al/C-2×1, the middle curve in Fig. 8(c) shows that the interfacial strength is 5 GPa, which is much smaller than the ideal strength of Al. Thus, failure at the interface is expected. However, the stress needed to separate Al/C-1×1:H is less than 0.4 GPa, which is 30 times lower than the ideal interfacial strength computed for Al/C-1×1, indicating the absence of bonds along Al/C-1×1:H. The integral of the stress-strain curve up to the fracture point gave 1.46 J/m^2 for Al/C-1×1, 0.58 J/m^2 for Al/C-2×1, and 0 for the Al/C:H interfaces, very close to the decohesion energy given by the energy calculations.

VII. DISCUSSION

After minimization, we found the total energy of the relaxed Al/C-2×1 is 1.43 J/m^2 higher than the relaxed Al/C-1×1. The corresponding interfacial energies are 3.78 J/m^2 for Al/C-2×1 and 2.35 J/m^2 for Al/C-1×1, respectively. This is surprising from the standpoint that the clean C(111) surface (with single dangling bonds) is unstable, and we have calculated the reconstructed C(111)-2×1 surface energy to be less than that for the C(111)-1×1 (unreconstructed) surface energy by 2.31 J/m^2. The fact that Al/C-1×1 has a lower energy implies that diamond dereconstructs upon exposure to Al to form stronger interface bonds, and the Al/C-1×1 interface is much more likely to be found experimentally. Therefore, within the constraints of the theoretical framework, our results for Al/C-1×1 are representative of Al and clean diamond interfaces, and our observation of Al transfer at Al/C(111)-1×1 but not at Al/C-1×1:H suggests that Al adheres to clean diamond but not to H-passivated diamond.

In addition to the work of adhesion measurements cited earlier, two experiments are of significance to the present work and serve as a backdrop for qualitative comparison. Hollman *et al.*[4] measured very low friction coefficients and wear rates in dry sliding tests involving CVD-diamond coated cemented carbide drills against Al. However, Schmid and Hector[62] observed nascent Al adhesion to nanometric-size pyramidal diamond indenters in dry asperity abrasion processes. At first sight, it seems that Al adhesion to the pyramidal diamond indenters but not to the diamond coating is contradictory. However, the indenter and coating materials had completely different surface structures; the (111) surface cut from diamond had a clean surface. On the other hand, the diamond coating grown in the CVD process was H passivated.[12] These observations are in general agreement with our observation that Al does not adhere to H-passivated diamond.

VIII. SUMMARY AND CONCLUSIONS

With the goal of understanding the role of diamond surface termination in adhesion and adhesive transfer at Al/diamond interfaces, we have conducted a first-principles study of two clean interfaces, viz., Al/C-1×1 and Al/C-2×1 and one H-terminated interface, i.e., Al/C-1×1:H. Adhesion was investigated via computation of W_{sep} for each interface. Adhesive transfer was investigated with a series of tensile straining calculations in which the interface was stretched to failure. These calculations provided constitutive laws that describe decohesion of the interfaces in terms of three regimes, viz., elastic stretching, incipient decohesion, and jump to separation.

The highest adhesion was found in Al/C-1×1, which contains the unstable diamond surface: we computed $W_{sep}=4.08$ J/m^2 for this interface. Application of tensile strain increments led to an interfacial strength of $\sigma_{max}=12$ GPa and revealed that this interface fails within the Al slab, with two Al layers transferring to the diamond surface. Contours of the electron localization function revealed covalent Al-C interface bonds. For Al/C-2×1, which contains the reconstructed diamond surface, we computed $W_{sep}=0.33$ J/m^2 and $\sigma_{max}=5$ GPa; decohesion occurs with no Al transfer. Interfacial bonding has a mixed covalent/metallic character with only one out of three Al surface atoms covalently bonded to

C. A comparison of the computed interfacial energies revealed that although it contains the reconstructed diamond surface, Al/C-2×1 is energetically less favorable than Al/C-1×1. This result suggests that there is no reconstruction of clean Al/diamond interfaces and, consequently, that Al adhesion to clean diamond surfaces will result in adhesive transfer of Al to diamond. For Al/C-1×1:H, we computed $W_{sep}=0.02$ J/m^2 and $\sigma_{max}=0.4$ GPa; strong covalent bonds between C and H preclude bond formation between Al and H with fracture occurring without adhesive transfer. Existing experimental results provide qualitative support of the results predicted herein.

ACKNOWLEDGMENTS

The authors wish to acknowledge Dr. Erich Wimmer, Dr. P. Saxe, and Dr. J. R. Smith for several stimulating discussions. Dr. T. W. Capehart and Dr. Y. T. Cheng provided valuable insights on diamond coating preparation and application.

[1] I.G. Batyrev, A. Alavi, and M.W. Finnis, Phys. Rev. B **62**, 4698 (2000).
[2] W.R.L. Lambrecht and B. Segall, J. Mater. Res. **7**, 696 (1992).
[3] J. Hoekstra and M. Kohyama, Phys. Rev. B **57**, 2334 (1998).
[4] S. Ogata and H. Kitagawa, J. Jpn. Inst. Met. **60**, 1079 (1996).
[5] D.J. Siegel, L.G. Hector, Jr., and J.B. Adams, Phys. Rev. B **65**, 085415 (2002).
[6] E.A.A. Jarvis, A. Christensen, and E.A. Carter, Surf. Sci. **487**, 55 (2001).
[7] D.J. Siegel, L.G. Hector, Jr., and J.B. Adams, Surf. Sci. **498**, 321 (2002).
[8] D.J. Siegel, L.G. Hector, Jr., and J.B. Adams, Acta Mater. **50**, 619 (2002).
[9] S.V. Dudiy, J. Hartford, and B.I. Lundqvist, Phys. Rev. Lett. **85**, 1898 (2000).
[10] A. Arya and E.A. Carter, J. Chem. Phys. **118**, 8982 (2003); **120**, 1142 (2004).
[11] X.G. Wang and J.R. Smith, Phys. Rev. Lett. **87**, 186103 (2001).
[12] H. Kawarada, Surf. Sci. Rep. **26**, 205 (1996).
[13] J.A. Garrido *et al.*, Appl. Phys. Lett. **82**, 988 (2003).
[14] P. Hollman, A. Alahelisten, T. Bjork, and S. Hogmark, Wear **179**, 11 (1994).
[15] A. Erdemir, Surf. Coat. Technol. **146**, 292 (2001); K.-H. Habig, *ibid.* **76–77**, 540 (1995); M. Berger and S. Hogmark, *ibid.* **149**, 14 (2002).
[16] K. Miyoshi, B. Pohlchuck, N.C. Whittle, L.G. Hector, Jr., and J. Adams, NASA Technical Report No. TM-1998-206638, 1998 (unpublished).
[17] Y.V. Naidich, in *Progress in Surface and Membrane Science*, edited by D.A. Cadenhead and J.F. Danielli (Academic Press, New York, 1981), Vol. 14; A.R. Ford and A.E. White, Chem. Eng. (Rugby, U.K.) **166**, 61 (1963).
[18] S.V. Pepper, J. Vac. Sci. Technol. **20**, 643 (1982).
[19] A. Scholze, W.G. Schmidt, and F. Bechstedt, Phys. Rev. B **53**, 13 725 (1996).
[20] K.C. Pandey, Phys. Rev. B **25**, 4338 (1982).
[21] G. Kern, J. Hafner, and G. Kresse, Surf. Sci. **366**, 445 (1996).
[22] Y. Qi and L.G. Hector, Jr., Phys. Rev. B **68**, 201403 (2003).
[23] G. Kresse and J. Hafner, Phys. Rev. B **49**, 14 251 (1994).
[24] G. Kresse and J. Furthmüller, Comput. Mater. Sci. **6**, 15 (1996).
[25] W. Kohn and L. Sham, Phys. Rev. **140**, A1133 (1965).
[26] R. Car and M. Parrinello, Phys. Rev. Lett. **55**, 2471 (1985).
[27] M.C. Payne, M.P. Teter, D.C. Allan, T.A. Arias, and J.D. Joannopoulos, Rev. Mod. Phys. **64**, 1045 (1992).
[28] W.H. Press, S.A. Teukolsky, W.T. Vetterling, and B.P. Flannery, *Numerical Recipes in* FORTRAN *90: The Art of Parallel Scientific Computing*, 2nd ed. (Cambridge University Press, Cambridge, 1996).
[29] G. Kresse and J. Hafner, Phys. Rev. B **48**, 13 115 (1993).
[30] G. Kresse and J. Furthmüller, Phys. Rev. B **54**, 11 169 (1996).
[31] J.P. Perdew, J.A. Chevary, S.H. Vosko, K.A. Jackson, M.R. Pederson, D.J. Singh, Phys. Rev. B **46**, 6671 (1992).
[32] P.E. Blöchl, Phys. Rev. B **50**, 17 953 (1994).
[33] A.M. Rappe, K.M. Rabe, E. Kaxiras, and J.D. Joannopoulos, Phys. Rev. B **41**, 1227 (1990).
[34] L. Kleinman and D.M. Bylander, Phys. Rev. Lett. **48**, 1425 (1987).
[35] H.J. Monkhorst and J.D. Pack, Phys. Rev. B **13**, 5188 (1976).
[36] M. Methfessel and A.T. Paxton, Phys. Rev. B **40**, 3616 (1989).
[37] P.E. Blöchl, O. Jepson, and O.K. Andersen, Phys. Rev. B **49**, 16 223 (1994).
[38] R.P. Feyman, Phys. Rev. **56**, 340 (1939).
[39] F.D. Murnaghan, Proc. Natl. Acad. Sci. U.S.A. **30**, 244 (1944).
[40] G. Grimvall, *Thermophysical Properties of Matter* (Elsevier, Amsterdam, 1999).
[41] Y. LePage and P. Saxe, Phys. Rev. B **65**, 104104 (2002).
[42] G. Kresse, Ph.D. Thesis, Technische Universität Wien, 1993.
[43] J.F. Nye, *Physical Properties of Crystals* (Oxford University Press, New York, 2001).
[44] L.G. Hector, Jr., J.F. Herbst, and T.W. Capehart, J. Alloys Compd. **353**, 74 (2003).
[45] E. Tatge and H.E. Swanson, *Standard X-Ray Diffraction Powder Patterns*, Natl. Bur. Stand. (U.S.) Circ. No. 539 (U.S. GPO, Washington, D.C., 1953), Vol. 359, p. 1.
[46] G. Simmons and H. Wang, *Single Crystal Elastic Constants and Calculated Aggregate Properties: A Handbook*, 2nd Ed. (MIT, Cambridge, MA, 1971).
[47] C. Kittel, *Introduction to Solid State Physics*, 7th ed. (Wiley, New York, 1996).
[48] See http://www.webelements.com
[49] See NIST Webbook, http://webbook.nist.gov/cgi
[50] J. Emsley, *The Elements*, 3rd ed. (Oxford University Press, New York, 1999).
[51] H.J. McSkimin and P. Andreatch, Jr., J. Appl. Phys. **43**, 2944 (1972).
[52] See IoffePhysico-technicalInstitute,Russia/, http://www.ioffe.rssi.ru/SVA/NSM/Semicond/Diamond/mechanic.html
[53] *Synthetic Diamond—Emerging CVD Science and Technology*, edited by K.E. Spear and J.P. Dismukes (Wiley, New York, 1994).

[54] J.C. Boettger, Phys. Rev. B **49**, 16 798 (1994).
[55] S. Hong and M.Y. Chou, Phys. Rev. B **57**, 6262 (1998).
[56] C. Kanai, K. Watanabe, and Y. Takakuwa, Phys. Rev. B **63**, 235311 (2001).
[57] R.E. Stallcup and J.M. Perez, Phys. Rev. Lett. **86**, 3368 (2001).
[58] J.E. Houston, G.E. Laramore, and R.L. Park, Science **185**, 258 (1974).
[59] A.D. Becke and K.E. Edgecombe, J. Chem. Phys. **92**, 5397 (1990).
[60] J.R. Smith, G. Bozzolo, A. Banerjea, and J. Ferrante, Phys. Rev. Lett. **63**, 1269 (1989).
[61] N.H. Macmillan, J. Mater. Sci. **7**, 239 (1972).
[62] S.R. Schmid and L.G. Hector, Jr., Wear **215**, 257 (1997).